Pushing the composition limit of anisotropic $Ge_{1-x}Sn_x$ nanostructures and determination of their thermal stability

Michael S. Seifner,[¥] Sergi Hernandez,[φ,Δ] Johannes Bernardi,[‖] Albert Romano-Rodriguez,[φ,Δ] Sven Barth[¥]*

[¥] TU Wien, Institute of Materials Chemistry, Getreidemarkt 9, 1060 Vienna, Austria.

[φ] MIND-MIND- Department of Electronics, Universitat de Barcelona (UB), Martí i Franquès 1, 08028 Barcelona, Spain.

[Δ] Institute of Nanoscience and Nanotechnology (IN2UB), Universitat de Barcelona (UB), Martí i Franquès 1, 08028 Barcelona, Spain

[‖] University Servicecenter for TEM (USTEM), TU Wien, Wiedner Hauptstrasse 8-10, 1040 Vienna, Austria.

ABSTRACT: $Ge_{1-x}Sn_x$ nanorods (NRs) with a nominal Sn content of 28% have been prepared by a modified microwave-based approach at very low temperature (140 °C) with Sn as growth promoter. The observation of a Sn-enriched region at the nucleation site of NRs and the presence of the low temperature α-Sn phase even at elevated temperatures support a template-supported formation mechanism. The behaviour of two distinct $Ge_{1-x}Sn_x$ compositions with high Sn content of 17% and 28% upon thermal treatment has been studied and reveal segregation events occurring at elevated temperatures, but also demonstrate the temperature window of thermal stability. In situ transmission electron microscopy investigations revealed a diffusion of metallic Sn clusters through the $Ge_{1-x}Sn_x$ NRs associated with temperatures where the material composition changes drastically. These results are important for the explanation of distinct composition changes in $Ge_{1-x}Sn_x$ and the observation of solid diffusion combined with dissolution and redeposition of $Ge_{1-y}Sn_y$ (x>y) exhibiting a reduced Sn content. Absence of metallic Sn results in increased temperature stability by ~70 °C for $Ge_{0.72}Sn_{28}$ NRs and ~60 °C for $Ge_{0.83}Sn_{17}$ nanowires (NWs). In addition, a composition-dependent direct bandgap of the $Ge_{1-x}Sn_x$ NRs and NWs with different composition is illustrated using Tauc plots.

Introduction

Group IV semiconductor nanowires (NWs) are potential building blocks for different fields of application including electronic and optoelectronic devices.[1] However, the performance of Si- and Ge-based materials in optics and photonics is limited by their indirect bandgap. Theoretical and experimental reports describe a modification of the Ge band structure to make direct gap emission more favorable by using tensile or uniaxial strain.[2, 3, 4] Alternatively, the light emission and absorption characteristics of Ge change dramatically, when a threshold concentration exceeds ~8-10 % Sn in $Ge_{1-x}Sn_x$ rendering it in a direct bandgap material which was experimentally observed[5, 6] and also calculated[7, 8]. $Ge_{1-x}Sn_x$ is compatible with CMOS processing based on Si technology and therefore an ideal candidate for infrared optoelectronics and optical devices, such as infrared lasers,[5, 9, 10, 11] photodetectors[12, 13] or light emitting diodes[14, 15, 16]. In addition, the electronic properties are also altered upon Sn incorporation in the Ge matrix which should result in an enhanced electron and hole mobility making $Ge_{1-x}Sn_x$ interesting for high-speed electronics.[17, 18, 19, 20, 21] An incorporation of Sn in the Ge lattice

in a bottom-up synthesis should be carried out under kinetic control, because the binary phase diagram reveals the low equilibrium solubility of Sn in Ge (<1 %).[22] Besides thin film growth studies and post-growth etching to prepare desired morphologies,[23] reports on $Ge_{1-x}Sn_x$ nanostructures are emerging.[24, 25, 26, 27, 28] Morphological control has been achieved creating core-shell Ge/$Ge_{1-x}Sn_x$[29] using Ge NWs as templates and non-template based metal-seed supported growth of $Ge_{1-x}Sn_x$ nanowires via gas-phase[30, 31] and solution–based synthesis[32, 33]. To date, the compositions vary in these reports on the growth of anisotropic $Ge_{1-x}Sn_x$ nanostructures with the highest values being in the range of 9-13 % Sn.[29, 30, 33] Moreover, a transition to a semimetallic behavior with interesting applications can be expected when the Sn content can be increased above 41 %[34]. Data confirming such high Sn concentrations in $Ge_{1-x}Sn_x$ with high crystallinity have only been rarely described in literature with limited information about their actual homogeneity with maximum Sn contents of ~30 %.[25, 26, 27, 35, 36, 37] The thermal stability of thin films with different composition is reported, but these reports do usually not cover higher tin contents >15 %, the heat treatment is limited to short

time, e.g. by rapid thermal annealing, and the films are usually highly strained.[38, 39, 40]

This paper provides insight in the formation mechanism of anisotropic $Ge_{1-x}Sn_x$ structures at temperatures as low as 140 °C leading to a Sn content of 28 %, while the formation of α-Sn for this low temperature process is elaborated. Two distinct compositions have been reliably synthesised with two different temperature profiles and pretreatment processes leading to Sn contents of ~17 % and ~28 % and without additional nucleation of branches or substructures. Thermal stabilities of these two alloy compositions are determined by variable temperature X-ray diffraction (XRD) and subsequent microscopy studies. Our study reveals the strong influence of metallic Sn on the thermal stability of the $Ge_{1-x}Sn_x$ materials. Infrared (IR) absorption was used to characterise the materials properties and clearly reveals the strong impact of direct bandgaps in the absorption spectra for both compositions.

Experimental

Chemicals:

Butyl lithium, hexamethyldisilazane, $SnCl_2$, 1,1,3,3-tetramethyldisiloxane, and $GeCl_4$ were purchased from Sigma Aldrich. All solvents were dried using standard procedures and stored over molecular sieve. All manipulations and syntheses have been conducted using Schlenk techniques or using argon filled glove box. $LiN(Si(CH_3)_3)_2$ was prepared in hexane and purified by sublimation under reduced pressure. The $GeCl_2 \cdot dioxane$ complex was prepared according to a published procedure.[41] The syntheses of $Sn(N(Si(CH_3)_3)_2)_2$ and $Ge(N(Si(CH_3)_3)_2)_2$ were prepared by a modified procedure published by Lappert et al. using salt metathesis reaction.[42]

Dodecylamine (98 %, Sigma Aldrich) was kept 2 h at 60 °C under dynamic vacuum and was distilled three times under reduced pressure. In the first distillation step high-molecular by-products were separated. For the second and third distillation 0.5-1 ml of $Sn(N(Si(CH_3)_3)_2)_2$ were added to 200 ml of dodecylamine to separate all undesired chemicals as high-molecular residue which would react with $Sn(N(Si(CH_3)_3)_2)_2$ and $Ge(N(Si(CH_3)_3)_2)_2$ in the following materials synthesis.

n-Octylamine was purified analogous to dodecylamine without reducing the pressure during distillation due to the low boiling point. Squalane (98 %, TCI) was distilled two times under reduced pressure.

Nanostructure preparation:

Ge NRs/NWs were grown in 10 ml glass cells (Anton Paar GmbH) at temperatures between 120-230 °C. The handling of the chemicals as well as the filling of the reaction vessels was carried out in a glove box under stringent precautions against water.

In a typical experiment, 2 ml of dodecylamine were transferred in a glass cell for microwave synthesis. Dodecylamine was kept very close to the melting point. First $Sn(N(Si(CH_3)_3)_2)_2$ and subsequently $Ge(N(Si(CH_3)_3)_2)_2$ was added to dodecylamine and the glass cell was sealed with a Teflon coated silicone cap. Independent on the ratio of $Sn(N(Si(CH_3)_3)_2)_2$ and $Ge(N(Si(CH_3)_3)_2)_2$ all samples prepared in this study have the same total concentration of 38 mM precursor to make a comparison possible. The vial was then transferred to the microwave reactor (Monowave 300; Anton Paar GmbH; wavelength 2.46 GHz) with an IR temperature control unit within 3 minutes. The precursor solution underwent a temperature programme and was cooled down by a gas stream afterwards. The synthesised structures were collected by adding toluene (3 ml) and subsequent centrifugation. The collected solid material was redispersed in toluene and centrifuged again to remove the dodecylamine. Another three times this step was repeated with ethanol and further three times with toluene. The product was stored under ambient conditions in toluene.

Further information about the pretreatment of the precursor mixture for the synthesis of $Ge_{1-x}Sn_x$ nanowires with 17 % Sn are given in our previous paper.[33] For the synthesis of $Ge_{1-x}Sn_x$ NRs with higher Sn content the following temperature programmes were chosen: Pretreatment 1 (PT1): (i) heat as fast as possible to 110 °C; (ii) cool down to 60 °C; (iii) hold for 10 min; (iv) heat as fast as possible to 140-160 °C; (v) hold temperature for 0-10 min; (vi) cool down to 55 °C. Pretreatment 2 (PT2): (i) heat as fast as possible to 60 °C; (ii) hold temperature for 40 min; (iii) heat as fast as possible to 140-160 °C; (v) hold temperature for 0-10 min; (vi) cool down to 55 °C.

Nanostructure characterisation:

The $Ge_{1-x}Sn_x$ NRs and NWs were analysed using a FEI Inspect F50 scanning electron microscope (SEM). The $Ge_{1-x}Sn_x$ NRs/NWs were deposited on lacey carbon copper grids (Plano) for transmission electron microscope (TEM) characterisation. In this study, a FEI TECNAI F20 operated at 200 kV and equipped with high angle annular dark field (HAADF) STEM and EDX detector was used. The elemental maps were recorded using the EDAX TEAM package and the quantification was calculated using the Ge(K) and Sn(L) signals. For the values included in the manuscript inherent limits in accuracy related to EDX have to be considered (±0.5%). The images were recorded and treated using Digital Micrograph software. *In situ* heating experiments in the TEM were performed using a Gatan heating holder 652.

The X-ray diffraction (XRD) patterns were recorded on a PANalytical X-Pert PRO PW 3050/60 in Bragg-Brentano geometry and Cu-Kα radiation. High-temperature XRD (HTXRD) measurements were carried out on a PANalytical MPD Pro in grazing incidence mode with an incidence angle of 4° and Cu-Kα radiation under hydrogen atmosphere. X-pert Highscore software was used for analysis of the measured data.

Transmission measurements were performed using the Perkin Elmer Frontier FT-IR spectrometer in mid-IR mode. The spectra were acquired from 220 cm^{-1} to 8000 cm^{-1}, with a 4 cm^{-1} resolution, using 64 scans. A reference spectrum of the substrate was also acquired under the

same conditions, thus allowing a determination of the NR and NW sample transmittance by rationing their spectrum against the one from the substrate. Then, the absorbance α (absorption coefficient times the thickness) was evaluated just by applying logarithm (i.e., -ln(T), where T is the transmittance). For the determination of the bandgap energy, we have employed the Tauc-plot method considering a direct bandgap of a material, which consist of a representation of $(\alpha h\nu)^2$ versus hν, being hν the energy of the incident photons: the intersection of the linear trend at high energies with the abscissa axis will provide the bandgap energy of the analysed material.

Results and Discussion

Low temperature growth regime

The microwave synthesis in dodecylamine has been previously described for synthesis temperatures of 230 °C.[33] A modified procedure has been developed in order to allow a controlled nucleation and growth of $Ge_{1-x}Sn_x$ nanostructures at temperatures as low as 140 °C requiring a certain pretreatment before the growth is initiated. Two pretreatment procedures (PT1 ~10 min and PT2 ~40 min) have been successfully applied and result in material with identical morphology and composition (Figure S1). These investigations also allow us to identify different intermediate structures in the evolution of NRs and NWs.

The structural evolution at these low temperatures includes the formation of globular particles, which convert into teardrops, heterodimeric structures and finally nanorods as shown in Figure 1a-d. Associated with the morphological changes, specific phases can be observed as shown in Figure 1e. The XRD patterns show α-Sn, β-Sn and Ge reflections with specific shift towards lower angles as expected for the formation of $Ge_{1-x}Sn_x$. The first crystalline phase that can be observed is β-Sn with a typical globular shape in the SEM image (Figure 1a), which is often observed for low melting metallic particles. This phase is present in all XRD patterns in Figure 1. The second diffractogram contains the typical low temperature, cubic α-Sn phase represented by the appearance of teardrop structures in addition to some remaining globular particles (Figure 1b). The α-Sn phase can be stabilised at higher temperatures (>13 °C) by the incorporation of Ge[43] or template effects on lattice matched substrates[44, 45], which could be both responsible for the appearance of α-Sn. The here observed data do not allow a definite assignment to either aforementioned triggers/processes for the phase transition from β-α Sn, but the incorporation of Ge is described *vide infra* suggesting that the actual Ge content is responsible for the stabilisation of this phase. Similarly, α-Sn has been also observed with other metal incorporation, such as Li.[46]

After 1.5 minutes first reflections associated to $Ge_{1-x}Sn_x$ are evident, which are more prominent after prolonged decomposition due to the extension of the $Ge_{1-x}Sn_x$ segment in the nanorods as can be expected from the SEM images (Figure 1c+d). The shift in the Ge peaks can be correlated to the concentration of Sn using the lattice constant of

the cubic phase of tin (α-Sn, 6.489 Å, JCPDS 00-005-0390), which is isostructural to cubic Ge (5.658 Å), according to Vegard's law. This calculated value is quite accurate for structures, where no strain from a substrate has to be taken into account;[25, 26, 27, 30] however, for highly accurate determination of the composition of surface bound epitaxial layers a small deviation is corrected by the bowing parameter which is highly dependent on the literature reports.[47, 48, 49] In an earlier report, we quantified the Sn concentration via EDX using the Sn(K) line, which leads to an underestimation of the actual Sn content in $Ge_{1-x}Sn_x$ NWs[33]. In addition, the large variation of the related Raman shift in literature on thin epitaxial films can be misleading. [50, 51, 52, 53]
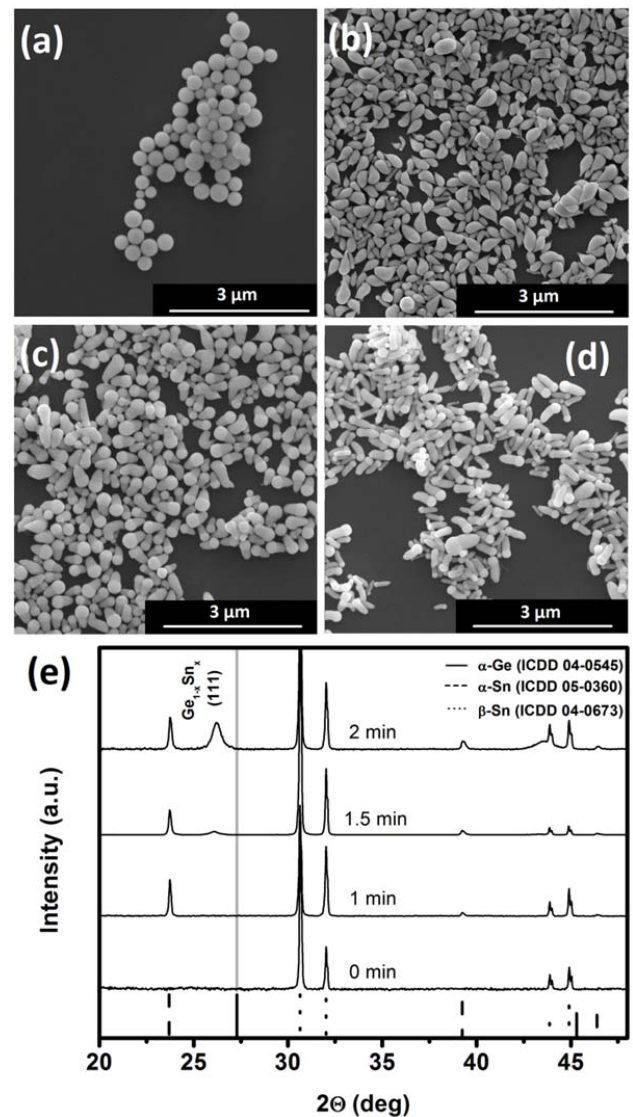

FIGURE 1 SEM images showing products obtained using PT1 and thermal decomposition at 140 °C for (a) 0 min, (b) 1 min, (c) 1.5 min and (d) 2 min. The XRD patterns in (e) correspond to the material shown in (a-d). The vertical grey line corresponds to the Ge (111) reflection of the reference, serving

as visual guide, and allows to clearly observe the large shift in the reflection for $Ge_{1-x}Sn_x$.

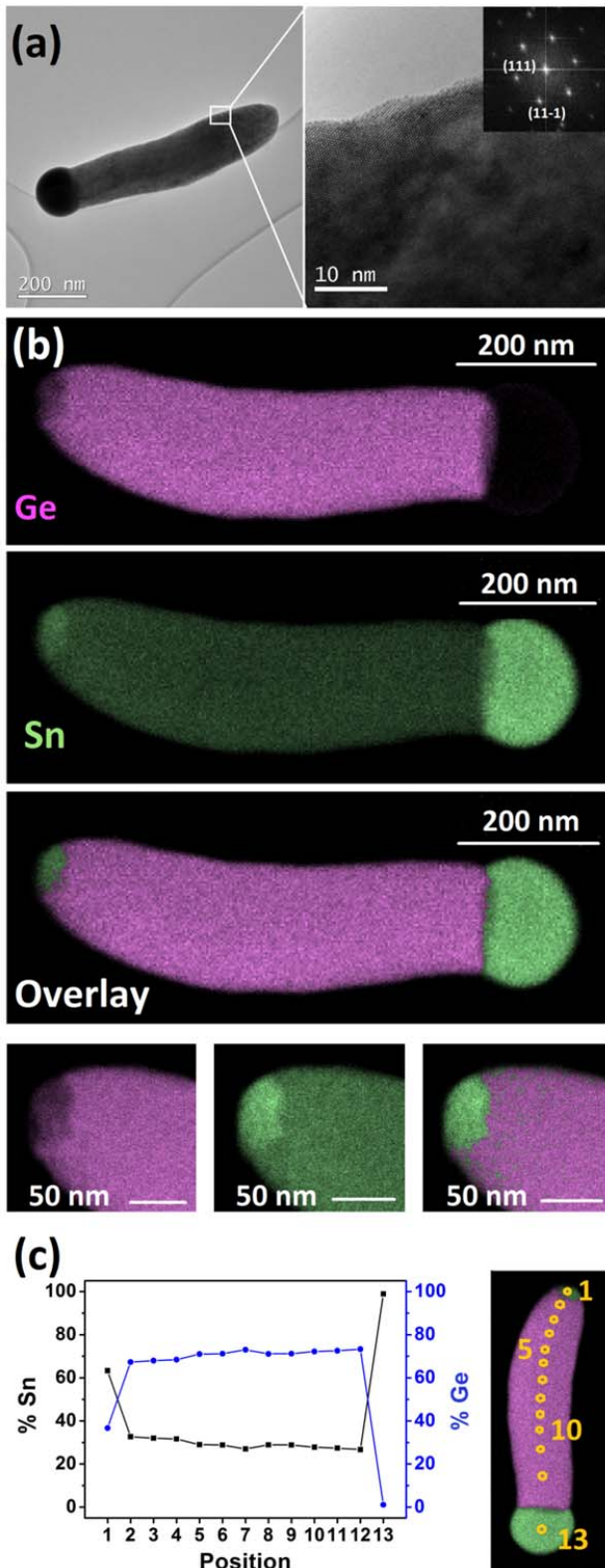The previously[33] not observed accumulation at the initial nucleation site is magnified and the mapping in higher resolution clearly shows a region with high Sn content. An overview of point EDX measurements in (c) shows the transition from a slightly higher concentration of ~32 % to 27.7±0.4 % segment (point 5-12) after ~ 150 nm from the Sn enriched nucleation site of the NR displayed in (b).

TEM images of NRs clearly show a quasi-hemispherical segment and the NR body with different diffraction contrast (Figure 2a). Focusing on the NR body by high resolution (HR)TEM reveals the high crystallinity, which is also illustrated in the sharp Fast Fourier transformation (FFT) pattern of Figure 2a. The local Sn concentration in the $Ge_{1-x}Sn_x$ NRs has been evaluated using scanning transmission electron microscopy (STEM) energy dispersive X-ray spectroscopy (EDX) mapping using the Sn(L) and the Ge(K) line for quantification. The elemental mapping reveals the homogeneous distribution of Sn in the Ge matrix without any sign of clustering in the NR body (Figure 2b).

The $Ge_{1-x}Sn_x$ NRs grown at 140 °C show two distinct sites of Sn enrichment located at both extremes on the NRs. The bigger globular part is located at the growth front of the NRs as described before for NWs grown at 230 °C, while a small section of Sn enrichment is located at the nucleation site. This is a general phenomenon for these NRs derived at 140°C as illustrated in additional STEM-EDX mappings of NRs in the supporting information (Figure S2). A transition zone of slightly higher Sn content (>32 %; 100-150 nm transition zone) can be found between this Sn-rich area and the constant $Ge_{0.72}Sn_{0.28}$ composition within the NR body. An overview of EDX point measurements is shown in Figure 2(c). The Sn-rich zone at the nucleation site can be associated to a remaining α-Sn segment acting as a template for the $Ge_{1-x}Sn_x$ phase formation. The Sn concentration determined by EDX in the NR body of 27.7±0.4 % (content according to XRD 27.5 %; abbreviated hereafter as $Ge_{0.72}Sn_{0.28}$), which is roughly 15 % Sn higher than previously reported values of ~12-13 % Sn in core-shell NWs[29] and 9 % Sn in NWs of constant diameter[30].

At slightly higher growth temperatures of 160 °C the aforementioned Sn-rich particle at the nucleation site can completely phase separate and act as a second growth seed for a thinner NR as shown in Figure 3. This thinner NR has a diameter of ~50 nm and the same composition as the thicker nanorod (Ø=210 nm) with 26.5 % Sn, while the initial nucleation area shows a higher Sn percentage (32 %). This comparison illustrates a diameter independent composition for NR diameters of 50-250 nm at these low temperatures and rather epitaxial growth on an initial seed with partial relaxation and formation of the most stable composition at the given growth conditions.

FIGURE 2 (a) TEM and HRTEM image of $Ge_{1-x}Sn_x$ NRs grown at 140 °C including the corresponding FFT image as an inset. The STEM-EDX mapping in (b) shows a homogeneous Sn distribution and an accumulation of Sn at both extremes.
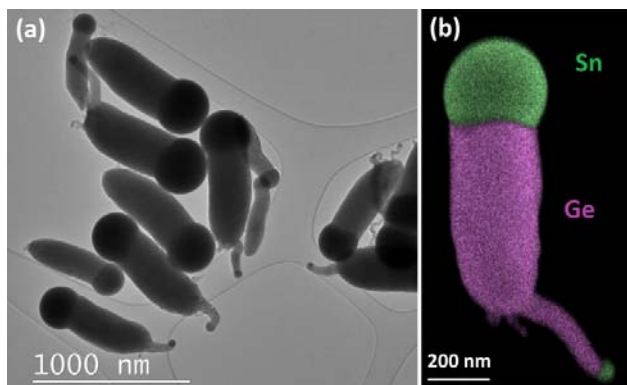
FIGURE 3 Decomposition of the precursor mixture at 160 °C using pretreatment PT1 leads to a secondary growth of a second NR from the initially formed Sn-rich segment described in figure 2. (a) TEM and (b) STEM-EDX image show the obtained structures.

Without the pretreatment the nanostructures tend to form NRs with secondary, "parasitic" structures protruding from the initial nucleation site and uncontrolled nucleation of undefined, branched structures as illustrated in Figure S3 are observed. In a separate set of experiments, the dodecylamine was substituted by n-octylamine and the growth was repeated under identical conditions with the same pretreatment at temperatures of 130-160 °C. The elongated structures contain an even higher Sn content in the NR body (32.1 ± 0.5 %Sn according to EDX, Figure S4) and could be interesting for applications taking advantage of semimetallic properties;[54] however the structures tend to form secondary nucleation centres at the surface leading to uncontrolled branching (especially at early stages of the $Ge_{1-x}Sn_x$ crystal formation with a nominal Sn content of 35.6 %), which can be related to different decomposition rates of the formed metalorganic intermediates and correlated changes in the nuclei formation and growth kinetics. The formation of the secondary nucleation sites can be most likely attributed to thermal instability of the $Ge_{1-x}Sn_x$ composition as described *vide infra*.

According to the here observed results, a growth mechanism for these NRs growing at 140 °C is proposed (Figure 4a). The pretreated precursor mixture contains homometallic Sn species leading to the formation of β-Sn particles as a first step. The β-Sn particles contain ≤0.4 % Ge averaged over the whole particle according to STEM-EDX analysis. Figure S5a shows the Ge predominantly accumulated at the Sn surface, while the majority of Ge can be expected to be distributed within the β-Sn particle at elevated temperatures and separation that occurs upon cooling. These globular β-Sn particles are converted to teardrop shaped α-Sn by additional gradual incorporation of Ge that stabilises this cubic Sn phase.[43] The α-Sn phase is expected to form via solid diffusion requiring a critical Ge concentration (~0.7-1.0 % according to EDX analyses of several particles similar to the one shown in Figure S5b). A critical parameter at this stage is the initially slow rate of Ge precursor decomposition leading to a gradual increase in Ge content. While the Ge concentration must be high enough for the conversion to α-Sn, the local concentration should be also low enough to avoid an initial nucleation of a $Ge_{1-x}Sn_x$ particle. A complete or a partial conversion to the α-Sn particles can be expected under growth conditions with the possibility of coexisting Sn phases. Unfortunately this growth stage could not be fully investigated due to potential material modification during the cooling of the material in the microwave process and no possibility of a rapid quenching with the used equipment. However, the presence of a α-Sn phase is important for the formation of NRs with such a high Sn content as discussed below.

Increased thermal input accelerates the decomposition kinetics of the precursor species and thus no α-Sn can be formed due to a quick oversaturation of the Sn particle and the subsequent nucleation of a $Ge_{1-x}Sn_x$ crystal (similar to a nucleus observed in Figure S5c formed at 180 °C). In addition, increased growth temperatures reduce the probability of an α-Sn phase formation. This indicates already that the exclusive nucleation / formation of the $Ge_{1-x}Sn_x$ segment with highest Sn content relies on a specific Ge supersaturation and the probability of an α-Sn phase forming at the given experimental conditions.

Further reaction at the growth temperature of 140 °C leads to the observation of a typical globular shaped β-Sn part in $Ge_{1-x}Sn_x$/Sn heterodimers. These structures can be formed by a destabilisation through an ongoing supersaturation of a fully developed α-Sn teardrop with formation of an associated $Ge_{1-x}Sn_x$ nucleus and a subsequent collapse of the crystal structure by diffusion processes. Another possibility that should not be neglected would be the nucleation of $Ge_{1-x}Sn_x$ in a possible Sn phase mixture with the α-Sn acting as template. Subsequent growth of the $Ge_{1-x}Sn_x$ segment proceeds through decomposition of more Ge-rich precursor species after the initial nucleus formation and appears to be a quick process according to Figure 1. The growth of the highly crystalline metastable $Ge_{1-x}Sn_x$ with this extremely high Sn content should be facilitated at low temperature due to reduced Sn incorporation at increasing temperatures.[55] The α-Sn phase can act as a template for epitaxial growth of highly Sn-rich $Ge_{1-x}Sn_x$ (mismatch to cubic Ge ~15 % for pure α-Sn) facilitating crystal growth of the thermodynamically unfavorable composition. Indication of a formation of $Ge_{1-x}Sn_x$ without any tensile strain and the most favourable constant composition at a given parameter set is observed ~100-150 nm from the nucleation seed where a constant composition is observed along the NRs. Figure S5d-f of the supporting information illustrates different stages of the NR evolution from the formed heterodimers with two distinct Sn areas present in all the different stages after the $Ge_{1-x}Sn_x$ segregation.

We do not consider the generally accepted solute trapping at step edges during the nanowire growth to be the major driving force for the formation of $Ge_{1-x}Sn_x$ at these low temperatures as suggested for other metastable compositions in NWs.[56, 57] A slightly modified process should

be at play because the step edge based growth typically also suggests that the nanowire growth can proceed with successive addition of bilayers through step flow process [58] and oscillating supersaturation during the layer formation.[59] The $Ge_{1-x}Sn_x$ NRs and NWs grown in these microwave processes do usually not show a sharp interface with a specific atomic plane terminating the semiconductor segment at the interface to the metal particle and thus the model might not be fully applicable.

These suggestions on the growth mechanism are based on the morphologies and phases observed after the cool down procedure and without information of processes occurring *in situ* during the growth. Thus the information about the initial stage before the $Ge_{1-x}Sn_x$/Sn heterodimer formation is not entirely clear and might require more experiments with modified setups allowing either *in situ* monitoring or rapid quenching.

The described growth regime differs from the 230 °C samples, because these 230 °C-derived NWs do not show additional secondary growth at the nucleation site nor a remaining Sn particle.[32] Moreover, the different pretreatment leads to a change in the ratio of the precursor species in the mixture.[32] Long term treatment for the growth at 230 °C does not lead to nucleation in the heating step similar to the here described scenario for the 140°C nucleation. The structure formation for the 230 °C growth takes exclusively place at the higher temperature regime which can be illustrated by different growth stages/lengths of these NWs. The structures are only observed after the high temperature growth cycle and thus the formation at lower temperatures in these specific sets of experiments can be excluded.

Observations described above for the growth of $Ge_{0.82}Sn_{0.28}$ at 140 °C do not correlate with the conventional Ge/Sn phase diagram (Figure S6). A traditional binary phase diagram is obtained under thermodynamic equilibrium conditions. Therefore, such diagrams are not suitable to explain a kinetically driven formation of metastable phases, such as $Ge_{1-x}Sn_x$ with high Sn contents, which differ significantly from the equilibrium composition. However, we coin a term for such a descriptive/schematic representation being a "phase map" that includes some kinetic effects/phase compositions. For a phase map as presented/suggested herein, we have to consider phases and compositions formed under a specific parameters set. In this specific case the formation of $Ge_{1-x}Sn_x$ with metastable composition as well as the either metastable or simply not under regular conditions observable α-Sn phase should be discussed.
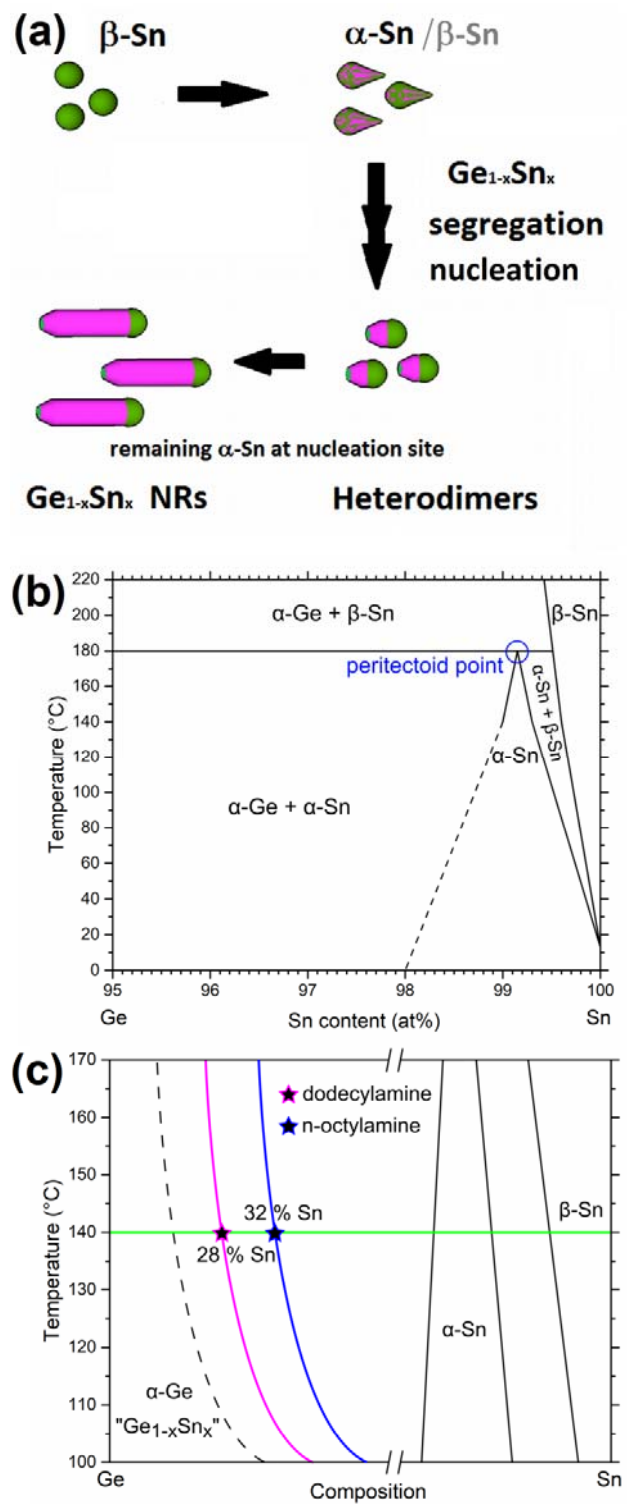

FIGURE 4 (a) Schematic representation of the low temperature nucleation of $Ge_{1-x}Sn_x$ NRs at 140 °C. The corresponding SEM images are displayed in Figure 1a-d and STEM-EDX images in Figure S5 support this suggestion. (b) A schematic representation of the Sn-rich side of a phase map and the assumption of a peritectoidic transformation and the existence of α-Sn at temperatures below 180 °C. (c) The phase map shows a suggested miscibility gap between the α-Sn

phase and an α-Ge phase with parameter-dependent composition variation ($Ge_{1−x}Sn_x$) for two solvents/ligands.

According to the here encountered phase evolution for Sn depending on the Ge content a representation of the Sn-rich side of the phase map should include a peritectoidic reaction (α-Sn ↔ α-Ge + β-Sn; a solid-solid reaction below 180 °C) (Figure 4b). However, the formation of this α-Sn phase relies on the incorporation of Ge atoms in the initial β-Sn lattice without segregation or Ge nucleus formation. This incorporation in the solid phase can be supported by the high mobility of surface atoms of low melting metals such as Sn and has a stabilising effect on the crystal phase. One can anticipate this peritectoidic α-Sn phase being a thermodynamically stable phase that is simply being not observed in the conventional heating and cooling experiments that are used for conceiving a phase diagram due to very slow reaction rates of two solid phases being β-Sn and α-Ge. Providing the Ge in atomic form speeds up this process and we can observe the phase in this study. In addition, energetic considerations suggest that there is only a small energy difference between the two Sn phases at the growth temperature of 140 °C.[60] Higher Ge contents will not be incorporated in α-Sn and α-Ge will nucleate. More reliable statements on α-Sn being thermodynamically stable or simply being a metastable phase would require more elaborate calculations, which also consider the high energy gain upon α-Ge crystal formation.

The existence of a miscibility gap between the two isostructural α-Sn and α-Ge phases showing no solid solubility over the full range of compositions could be related to early predictions by Hume-Rothery.[61] Stability issues can be related to the size differences of Sn and Ge, which is in this case ~15% representing a threshold value between the existence of solid solutions over a wide composition range and the occurrence of a large miscibility gap associated with low solubility <1% as observed in the Ge/Sn phase diagram.[61] A threshold for maximum Sn composition of the stable $Ge_{1-x}Sn_x$ alloy should be dependent on growth kinetics and growth temperature as schematically illustrated on the Ge-rich side in the phase map in Figure 4c. Our phase map suggests the formation of the α-Sn phase with a miscibility gap towards an α-Ge phase, representing the metastable $Ge_{1-x}Sn_x$ solid solution with compositions associated to growth kinetics and growth temperature. The purple, blue and dashed lines represent the max. $Ge_{1-x}Sn_x$ composition obtained for three specific parameter sets. Since growth kinetics are very important during the $Ge_{1-x}Sn_x$ crystal growth, e.g. with a solute trapping model in the case of nanowire growth, a higher/lower growth rate could result in a material with higher/lower Sn content. At the same time a temperature-dependent factor has to be considered for the phase map with a known tendency of diminishing Sn incorporation in $Ge_{1-x}Sn_x$ with increasing temperature.[55] The isothermal line at 140 °C in Figure 4c traverses the schematic purple and blue transition lines of maximum Sn content in the $Ge_{1-x}Sn_x$ alloy. These crossing points

represent the composition in $Ge_{0.72}Sn_{0.28}$ NR and $Ge_{0.68}Sn_{0.32}$ NWs for the same set of parameters (pretreatment and temperature profile) but different solvent and ligands of the precursors as described *vide supra*.

Thermal Stability of $Ge_{1-x}Sn_x$ NRs and NWs

In order to investigate the stability of anisotropic $Ge_{1-x}Sn_x$ structures with very high tin content (17 and 28 % as starting compounds), variable high temperature (HT) XRD experiments in the temperature range of 120-500 °C have been performed. To the best of our knowledge there is no report available on the thermal stability of $Ge_{1-x}Sn_x$ material, which is also in contact with a metallic phase.

In a first set of experiments $Ge_{0.83}Sn_{0.17}$ NWs have been prepared as described before[33] and a thin film of the NWs has been heated while recording the XRD patterns. The temperature is increased in 10 °C steps and the temperature is kept at the temperature for 10 mins before the measurement is started, which takes 20 mins. Therefore changes over time can have an uncertainty of ~10 °C if the effects are only observed after an initial delay. The β-Sn reflections can be considered as an internal standard until it melts at 230 °C. The shifted Ge reflections due to the enlarged unit cell upon the incorporation of Sn have to be considered for the stability tests since the shift is directly related to the composition by Vegard's law. Figure 5 shows no changes in the position of the reflections up to temperatures of 190 °C. At 200 °C the reflection broadens towards higher angles and a new composition with lower Sn content is observed (~6 % Sn). With further increase of temperature a continuous decrease of Sn content is observed and at 500 °C only 3.5 % Sn is left in the structure. The $Ge_{0.83}Sn_{0.17}$ is stable for at least 6 h at 160 °C without any noticeable changes in the XRD patterns (Figure S7), while at 180 °C the compound shows a noticeable onset of decomposition after 1h with Sn segregation and a shift in the reflection maxima to the aforementioned ~6 % Sn composition (Figure S8).
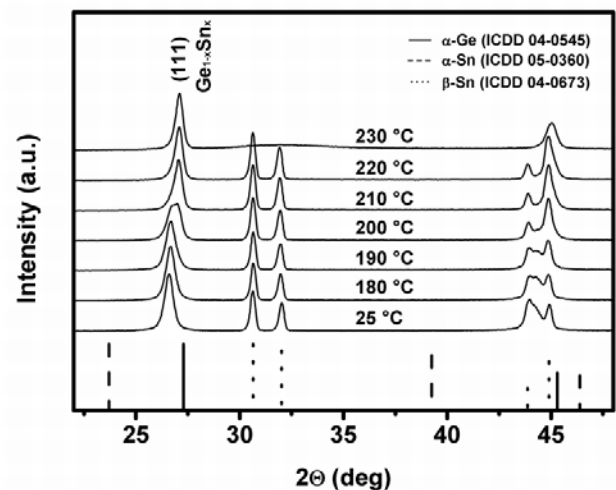
FIGURE 5 Variable temperature XRD showing the phase and evolution of the position of reflections in the temperature range 25-230 °C for $Ge_{0.83}Sn_{0.17}$ NWs.

The $Ge_{0.72}Sn_{0.28}$ NRs have been investigated as described before in the temperature range 120-500 °C (Figure 6a). No changes in the XRD patterns are observed up to 150 °C. A shoulder of the Ge (111) reflection evolves towards higher 2Θ angles at 160 °C and the signal clearly splits at 170 °C into two reflections with a new composition of $Ge_{0.90}Sn_{0.10}$ and the original $Ge_{0.72}Sn_{0.28}$ composition. At temperatures of 180-190 °C a shoulder representing the higher tin concentration is still present with diminishing intensity while only one reflection representing ~6 % Sn remains at 210 °C. This composition is very close to the value observed for the $Ge_{0.83}Sn_{0.17}$ starting material containing ~6 % at the same temperature. An identical value of 3.5 % Sn is observed for both starting compounds after temperature treatment at 500°C for 30 min and prior ramping as described for all variable temperature experiments. The 3D representation of the significant temperature window is illustrated in Figure 6b and shows in addition to the shift of the $Ge_{1-x}Sn_x$ (111) reflection an increase in the β-Sn content, which can be expected upon thermally induced spinoidal decomposition of crystalline $Ge_{1-x}Sn_x$ in a material $Ge_{1-y}Sn_y$ with lower Sn content (x>y) and the segregation of Sn. Since these relevant conversion temperatures are below the melting point of Sn a solid diffusion can be expected.

The onset of thermal decomposition is represented by the appearance of a shoulder of the Ge (111) reflection towards higher angles starting at temperatures of 160 °C in Figure 6. However, the as prepared $Ge_{0.72}Sn_{0.28}$ composition decomposes slowly at a static temperature of 140° (Figure 6c and S9) and held for 6 h. The onset of the decomposition requires time and since the temperature is only held for 30 min at each temperature in the variable temperature study in Figure 6a, this effect is only observed at higher temperatures. An unchanged composition and thus associated stability of $Ge_{0.72}Sn_{0.28}$ is observed at 120° for 6h as illustrated in Figure 6c and S10. The shift in the XRD pattern towards higher angles associated with a material conversion to $Ge_{1-x}Sn_x$ with lower Sn content in the isothermal heating experiments shows an exponential decay of the $Ge_{0.72}Sn_{0.28}$ starting compound after an initial incubation period. An example of this behaviour is shown in Figure S11 for a 6h heating cycle of as grown $Ge_{0.72}Sn_{0.28}$ NRs at 150 °C.
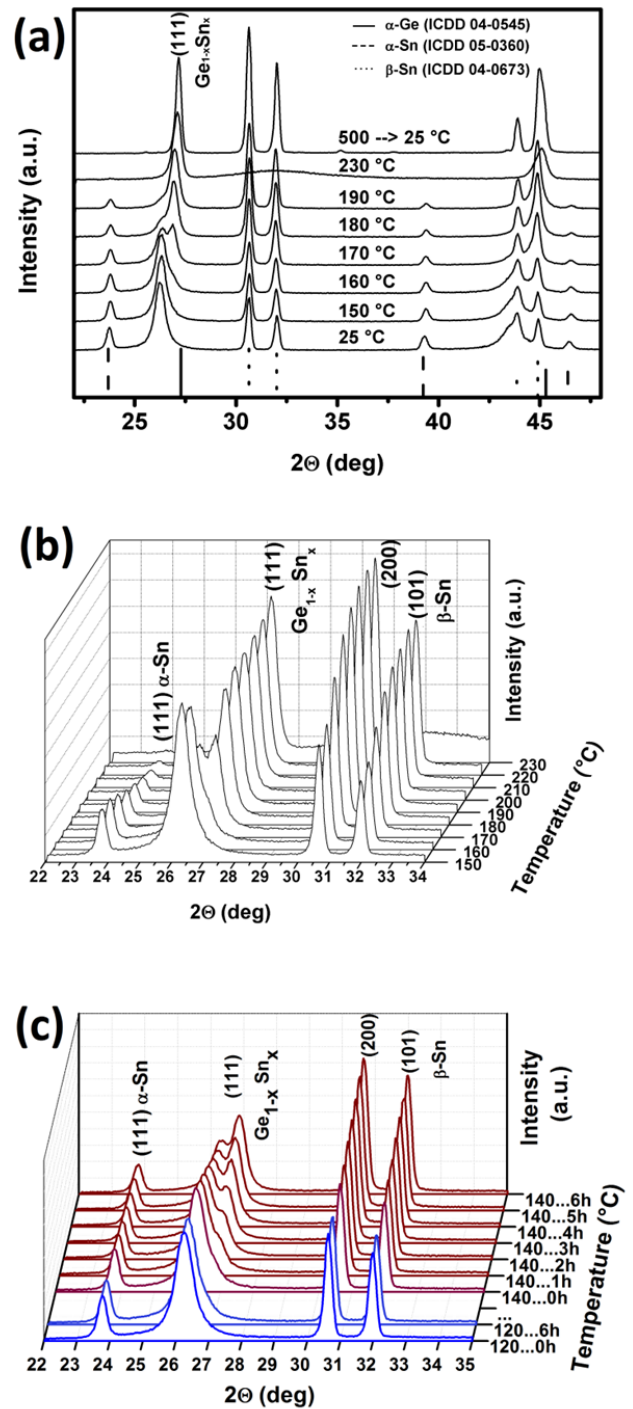

FIGURE 6 (a) Variable temperature XRD showing the phase evolution in the temperature range 25-230 °C and the XRD pattern for 500 °C treated sample cooled down to 25 °C) starting with $Ge_{0.72}Sn_{0.28}$ NRs. A 3D representation of the most interesting region for the phase evolution is shown in (b). the XRD patterns in (c) show the static temperature treatment at 120 °C (blue) and 140 °C (brown) for $Ge_{0.72}Sn_{0.28}$ NRs as starting compound.

We assign the peak splitting to the destabilisation of the $Ge_{0.72}Sn_{0.28}$ and related gain of lattice energy by the formation of more thermodynamically favourable composi-

tion, which requires additional energy for the conversion by diffusing species. Hence the decomposition and rearrangement of the Ge lattice should be simpler in the $Ge_{0.72}Sn_{0.28}$ sample because approximately every fourth atom in the cubic lattice is a Sn atom. After the splitting of the signal and temperatures above 160 °C the subsequent segregation of Sn is a gradual effect. Theory predicts that the number of defects with Sn in octahedral configuration increases with growth temperature and therefore the alloy should be less stable due to Sn in sixfold coordination and thus contributing to Sn segregation.[62] However, extended X-ray absorption fine structure investigations on $Ge_{1-x}Sn_x$ with $x_{max} = 13$ % illustrate that Sn preferentially resides on substitutional sites and no indices of this sixfold coordination are observed.[49] In addition, the here presented low synthesis temperature and the well-matched values for XRD and EDX results should account for mainly substitutional incorporation of Sn in the cubic lattice also for the high Sn content. Future studies will be focused on evaluating the nature of Sn coordination in the $Ge_{1-x}Sn_x$ NRs and NWs. It should be noted that the α-Sn phase is prevails up to 220°C and the reflections merely show a decrease of intensity above 180 °C before finally melting at 230 °C. The total α-Sn content is a combination of α-Sn teardrop particles as well as the small particle in the NRs at the nucleation site. High temperature stability of the α-Sn phase is also observed for epitaxial layers[63] (up to 130 °C) and for α-Sn confined in nanotubes with melting temperatures up to 700 °C,[64] which is ~470 °C above the melting temperature of β-Sn.

The segregation of Sn from the $Ge_{1-x}Sn_x$ NRs and NWs upon temperature treatment should result in morphological changes. All samples heated to high temperatures of 500 °C clearly show the formation of additional Sn particles on individual structures or a network connected by liquefied drops on locations of initially high density of NRs or NWs (Figure S12 a+b and S13 a+b). Even more interesting is the fate of segregated Sn related to obvious changes in the $Ge_{1-x}Sn_x$ composition below the melting temperature of Sn at 232 °C. According to the XRD data, the volume fraction of β-Sn increases and therefore we conclude that new evolving particles should be β-Sn. Changes cannot be explained by the bulk investigations and therefore in situ experiments have been performed to image a potential diffusion process.

In situ imaging in the TEM during heating cycles up to nominal 220 °C with a temperature controllable grid holder have been carried out. Videos show several processes during the heat treatment with clear similarities between processes observed in two $Ge_{0.72}Sn_{0.28}$ NRs. Video 1 is also used in figure 7, while another NR is imaged in videos 2+3 in the supplementary information. In a first step during heat treatment the hemispherical Sn seed grows slightly and the initial interface between the terminating Sn particle and the initial $Ge_{0.82}Sn_{28}$ segment changes on the left in Figure 7b. A mass diffusion can be observed by migrating species with different diffraction contrast towards the initial nucleation side (Figure 7c). As soon as this diffusing species reaches the initial nuclea-

tion site with the α-Sn nucleus, a sudden but permanent change in diffraction contrast takes place. However, the bulk/subsurface diffusion continues and further locations with varying diffraction contrast appear along the NR with some mobility. During the diffusion the Sn volume and thus the diffusing mass with different diffraction contrast increases due to a collection of Sn from the phase segregation (Figure 7e+f). The diffusion appears to be within the structural boundaries and the general shape before and after the temperature treatment remains the same. In addition, the conversion of $Ge_{1-x}Sn_x$ to material with lower Sn content could be related to an epitaxial growth of $Ge_{1-y}Sn_y$ (y<x) by redeposition from the migrating β-Sn segment (with higher volume fraction observed in the XRD studies *vide supra*). Moreover, the onset of the diffusion process seems to originate exclusively at the bigger Sn particle, which points towards the importance of the initial Sn/ $Ge_{1-x}Sn_x$ interface for this low temperature process being initiated.
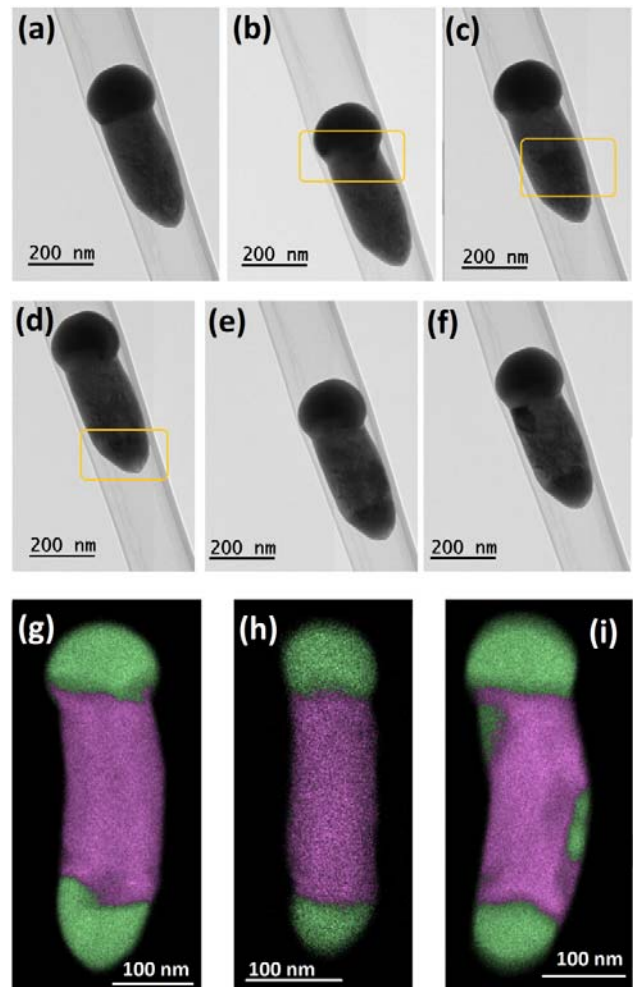

FIGURE 7 (a-f) TEM images obtained under temperature treatment using $Ge_{0.72}Sn_{0.28}$ NRs showing different steps in the phase segregation process which is imaged at nominal temperature of 200 °C of the holder and TEM grid. STEM-EDX images after temperature treatment for 10 min at 220 °C (g+h) in the TEM and (i) for a sample heated to 180 °C in squalane for ~20 min.

It is noteworthy that all these processes take place below the melting point of Sn (232 °C). $Ge_{0.82}Sn_{28}$ NRs treated in the TEM at 220°C for ~10 min and prior diffusion at 200 °C show preferentially Sn enrichment at the two extremes (Figure 7 g+h), while treatment for 20 mins at 180 °C in squalane shows more large patches of Sn enriched regions between the extremes(Figure 7 i). The NRs do not show distinct morphological changes in the SEM images before and after the temperature treatment (Figure S11c+d). TEM images of these NRs also show predominantly two darker segments at the extremes due to a different diffraction contrast, which have not been observed in as-grown samples. More examples for the formation of phase separated Sn patches are shown in Figure S11e-g, but less of the obvious Sn regions between the two extremes are observed in STEM-EDX images when the samples have been treated at higher temperatures. The reason for shape retention could be either the surface termination with amino functionalities, a slight surface oxidation layer or simply and most likely the bulk conversion/diffusion at these temperatures below the melting point of the elements involved. STEM-EDX images help to identify the segments composition. The $Ge_{1-x}Sn_x$ segment is not as defined any more suggesting also Ge diffusion and rearrangement processes (Figure 7g-i). The aforementioned mass transport is most likely initiated by a solution/redeposition process involving the diffusing β–Sn precipitate. The redeposited material contains less Sn in the Ge host structure and therefore the process is driving towards the thermodynamically favored Ge-rich lattice and a gain in lattice energy during the process can be expected. The redeposition/recrystallisation of $Ge_{1-y}Sn_y$ (x>y) is evidenced and most obvious by comparing the Ge mapping after the temperature treatment with the initial distribution (Figure S12e-h). A striking difference is visible at the initial nucleation site, where no Ge can be found after this process, and at the sites of the Sn patches along a NR where the Ge is completely replaced by Sn.

Differences in thermal stability of these structures when compared to other studies on $Ge_{1-x}Sn_x$ should be mentioned. The most important difference is the presence of the Sn metal, which can dissolve and recrystallise $Ge_{1-x}Sn_x$ while a metal has first to be formed when pure $Ge_{1-x}Sn_x$ decomposes and Sn segregates. This process of spinoidal decomposition requires a partial breakdown of the crystalline structure and thus more thermal energy has to be provided to overcome the lattice energy. Thus a removal of the Sn seed material from the NRs and NWs by exposure to 5 % hydrochloric acid for 5 min should lead to increased thermal stability. Figure S13 compares variable temperature XRD results of $Ge_{0.72}Sn_{0.28}$ NRs with and without the Sn seeds demonstrating the expected increased thermal stability with temperatures up to ~220 °C without decomposition, which is ~70 °C above the onset of a material conversion in the presence of Sn. A similar measurement using $Ge_{0.83}Sn_{0.17}$ NWs illustrate the same effect and stability up to 250 °C (vs. ~190 °C with Sn seeds in Figure 5 and for comparison without Sn in Figure S14). Temperature stability for extended time is usually ob-

served ~30°C below these values as shown *vide supra*. The here presented results can nicely explain the low temperature crystallisation of amorphous $Ge_{1-x}Sn_x$ layers from a laser annealed region forming highly crystalline $Ge_{1-x}Sn_x$ material.[65] This process resembles metal induced crystallisation of Ge occurring at higher temperatures[66], but leads to a metastable material composition.

Bulk Ge exhibits a fundamental indirect bandgap of 0.67 eV and a direct gap at 0.80 eV. Incorporation of Sn in the Ge crystal reduces both energy gaps, but the direct one to a larger degree than the indirect. Therefore, a direct semiconductor material is expected for the high tin contents described herein. In order to demonstrate the optical bandgap of the not thermally degraded $Ge_{1-x}Sn_x$ material, Figure 8 demonstrates the direct bandgap of $Ge_{0.72}Sn_{0.28}$ NRs and $Ge_{0.83}Sn_{0.17}$ NWs described herein. From IR absorption experiments a Tauc plot was prepared to determine the bandgap energy. A Tauc plot is a common way to determine the optical bandgap of semiconductors.

A determination of the bandgap in the material is achieved by plotting $(\alpha h v)^n$ vs hv and relating the factor n to an indirect (n = ½) or direct (n = 2) bandgap and the absorption coefficient (α).[67, 68] Approximate bandgaps of 0.29 eV for $Ge_{0.72}Sn_{0.28}$ NRs and 0.40 eV for $Ge_{0.83}Sn_{0.17}$ NWs were determined by extrapolating a tangential line from the linear portion of the Tauc plot to the abscissa. The direct bandgaps observed in these NRs and NWs are far below the usual bandgaps of Ge, which is expected for a successful incorporation of Sn in $Ge_{1-x}Sn_x$ above ~9% for a relaxed material and could be the indication that these NRs and NWs being indeed direct bandgap materials.[34] More detailed physical characterisation of the presented materials is out of the scope of this paper.
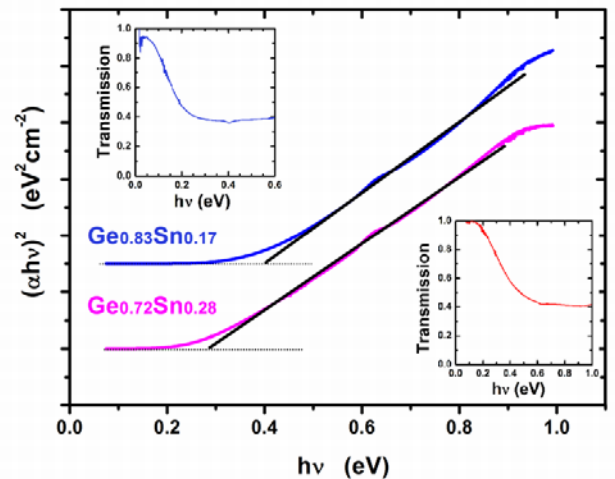

FIGURE 8 Tauc plot from IR absorption (insets) used to determine the direct bandgap energy of the NRs and NWs.

CONCLUSIONS

A low temperature growth at 140 °C for the formation of $Ge_{1-x}Sn_x$ NRs with a very high Sn content of 28% has been established. The typical low temperature α-Sn phase has been observed during the formation of the NRs and all the anisotropic structures remained a Sn-rich region at the nucleation site, which cannot be observed at nucleation at higher temperatures. Therefore we propose a growth mechanism for this particular set of parameters that is based on a Ge-stabilised α-Sn intermediate. Moreover, the thermal stability of two sets of NRs and NWs with different Sn content has been investigated via XRD and the data reveal decomposition at low temperature that has to be considered for the determination of their physical properties as well as the potential device operation. In addition, the low temperature decomposition of $Ge_{1-x}Sn_x$ appears to be related to a solid diffusion of Sn asobserved as mobile sections with different diffraction contrast during in *situ* TEM annealing experiments. The segregated Sn accumulates at low temperatures at the extremes of NRs and also as patches in between. The continuous release of Sn accompanied by the formation of crystalline $Ge_{1-x}Sn_x$ with lower Sn content and also spacial distribution of the elements suggest dissolution and recrystallisation events facilitated by diffusing Sn. Removal of the metallic Sn from the $Ge_{1-x}Sn_x$ results in enhanced stability towards thermal decomposition by ~70 °C for $Ge_{0.72}Sn_{0.28}$ NRs and ~60 °C for $Ge_{0.83}Sn_{0.17}$ NWs. Finally, a direct bandgap in the starting materials with such high Sn contents has been demonstrated via absorption experiments and the use of graphical illustration in Tauc plots.

ASSOCIATED CONTENT

Supporting Information. Additional SEM, TEM, EDX and XRD data are provided. Moreover, a video for the phase separation in the TEM is supplied. This material is available free of charge via the Internet at http://pubs.acs.org.

AUTHOR INFORMATION

Corresponding Author

* S. Barth, E-mail: sven.barth@tuwien.ac.at; Fax: +43 158801 165 99; Tel: +43 158801 165 207.

ACKNOWLEDGMENT

REFERENCES

[1] Barth, S.; Hernandez-Ramirez, F.; Holmes, J. D.; Romano-Rodriguez, A. Synthesis and applications of one-dimensional semiconductors. *Prog. Mater. Sci.* **2010**, *55*, 563.

[2] Nam, D.; Sukhdeo, D.; Cheng, S.-L.; Roy, A.; Chih-Yao Huang, K.; Brongersma, M.; Nishi, Y.; Saraswat, K. Electroluminescence from strained germanium membranes and implications for an efficient Si-compatible laser. *Appl. Phys. Lett.* **2012**, *100*, 131112.

[3] Jain, J. R.; Hryciw, A.; Baer, T. M.; Millerdavid, A. B.; Brongersma, M. L.; Howe, R. T. A micromachining-based technology for enhancing germanium light emission via tensile strain. *Nat. Photonics* **2012**, *6*, 398.

[4] Suess, M. J.; Geiger, R.; Minamisawa, R. A.; Schiefler, G.; Frigerio, J.; Christina, D.; Isella, G.; Spolenak, R.; Faist, J.; Sigg, H. Analysis of enhanced light emission from highly strained germanium microbridges. *Nat. Photonics* **2013**, *7*, 466.

[5] Wirths, S.; Geiger, R.; Von Den Driesch, N.; Mussler, G.; Stoica, T.; Mantl, S.; Ikonic, Z.; Luysberg, M.; Chiussi, S.; Hartmann, J. M.; Sigg, H.; Faist, J.; Buca, D.; Grützmacher, D. Lasing in direct-bandgap GeSn alloy grown on Si. *Nat. Photonics* **2015**, *9*, 88.

[6] Ghetmiri, S. A.; Du, W.; Margetis, J.; Mosleh, A.; Cousar, L.; Conley, B. R.; Domulevicz, L.; Nazzal, A.; Sun, G.; Soref, R. A.; Tolle, J.; Li, B.; Naseem, H. A.; Yu, S.-Q. Direct-bandgap GeSn grown on silicon with 2230 nm photoluminescence. *Appl. Phys. Lett.* **2014**, *105*, 151109.

[7] Lu Low, K.; Yang, Y.; Han, G.; Fan, W.; Yeo, Y.-C. Electronic band structure and effective mass parameters of $Ge_{1-x}Sn_x$ alloys. *J. Appl. Phys.* **2012**, *112*, 103715.

[8] Gupta, S.; Chen, R.; Magyari-Kope, B.; Lin, H.; Yang, B.; Nainani, A.; Nishi, Y.; Harris, J. S.; Saraswat, K. C. (2011). GeSn technology: Extending the Ge electronics roadmap. Technical Digest - International Electron Devices Meeting, IEDM.

[9] Stange, D.; Wirths, S.; Geiger, R.; Schulte-Braucks, C.; Marzban, B.; Von Den Driesch, N.; Mussler, G.; Zabel, T.; Stoica, T.; Hartmann, J.-M.; Mantl, S.; Ikonic, Z.; Grützmacher, D.; Sigg, H.; Witzens, J.; Buca, D. Optically Pumped GeSn Microdisk Lasers on Si. *ACS Photonics* **2016**, *3*, 1279.

[10] Al-Kabi, S.; Ghetmiri, S. A.; Margetis, J.; Pham, T.; Zhou, Y.; Dou, W.; Collier, B.; Quinde, R.; Du, W.; Mosleh, A.; Liu, J.; Sun, G.; Soref, R. A.; Tolle, J.; Li, B.; Mortazavi, M.; Naseem, H. A.; Yu, S.-Q. An optically pumped 2.5 μm GeSn laser on Si operating at 110 K. *Appl. Phys. Lett.* **2016**, *109*, 171105.

[11] Buca, D.; Von Den Driesch, N.; Stange, D.; Wirths, S.; Geiger, R.; Braucks, C. S.; Mantl, S.; Hartmann, J. M.; Ikonic, Z.; Witzens, J.; Sigg, H.; Grutzmacher, D. (2017). GeSn lasers for CMOS integration. Technical Digest - International Electron Devices Meeting, IEDM.

[12] Conley, B. R.; Margetis, J.; Du, W.; Tran, H.; Mosleh, A.; Ghetmiri, S. A.; Tolle, J.; Sun, G.; Soref, R.; Li, B.; Naseem, H. A.; Yu, S.-Q. Si based GeSn photoconductors with a 1.63 A/W peak responsivity and a 2.4 μm long-wavelength cutoff. *Appl. Phys. Lett.* **2014**, *105*, 221117.

[13] Pham, T. N.; Du, W.; Conley, B. R.; Margetis, J.; Sun, G.; Soref, R. A.; Tolle, J.; Li, B.; Yu, S. Q. Si-based $Ge_{0.9}Sn_{0.1}$ photodetector with peak responsivity of 2.85 A/W and longwave cutoff at 2.4 μm. *Electronics Letters* **2015**, *51*, 854.

[14] Tseng, H. H.; Wu, K. Y.; Li, H.; Mashanov, V.; Cheng, H. H.; Sun, G.; Soref, R. A. Mid-infrared electroluminescence from a $Ge/Ge_{0.922}Sn_{0.078}/Ge$ double heterostructure p-i-n diode on a Si substrate. *Appl. Phys. Lett.* **2013**, *102*, 182106.

[15] Gupta, J. P.; Bhargava, N.; Kim, S.; Adam, T.; Kolodzey, J. Infrared electroluminescence from GeSn heterojunction diodes grown by molecular beam epitaxy. *Appl. Phys. Lett.* **2013**, *102*, 251117.

[16] Chang, C.; Chang, T.-W.; Li, H.; Cheng, H. H.; Soref, R.; Sun, G.; Hendrickson, J. R. Room-temperature 2-μm GeSn P-I-N homojunction light-emitting diode for inplane coupling to group-IV waveguides. *Appl. Phys. Lett.* **2017**, *111*, 141105.

[17] Schulze, J.; Blech, A.; Datta, A.; Fischer, I. A.; Hähnel, D.; Naasz, S.; Rolseth, E.; Tropper, E.-M. Vertical Ge and GeSn heterojunction gate-all-around tunneling field effect transistors. *Solid-State Electron.* **2015**, *110*, 59.

[18] Kouvetakis, J.; Menendez, J.; Chizmeshya, A. V. G. Tin-based group IV semiconductors: New Platforms for Opto- and Microelectronics on Silicon. *Ann. Rev. Mater. Res.* **2006**, *36*, 497.

[19] Sau, J. D.; Cohen, M. L. Possibility of increased mobility in Ge-Sn alloy system. *Phys. Rev. B* **2007**, *75*, 045208.

[20] Lei, L.; Renrong, L.; Jing, W.; Jun, X. Investigation on the effective mass of Ge 1– x Sn x alloys and the transferred-electron effect. *Appl. Phys. Express* **2015**, *8*, 031301.

[21] Wang, S.; Zheng, J.; Xue, C.; Li, C.; Zuo, Y.; Cheng, B.; Wang, Q. Device simulation of GeSn/GeSiSn pocket n-type tunnel field-effect transistor for analog and RF applications. *Superlattices Microstruct.* **2017**, *111*, 286.

[22] Olesinski, R. W.; Abbaschian, G. J. The Ge–Sn (Germanium–Tin) system. *Bull. Alloy Phase Diagrams* **1984**, *5*, 265.

[23] Sukhdeo, D. S.; Hai, L.; Donguk, N.; Ze, Y.; Vulovic, B. M.; Gupta, S.; Harris, J. S.; Dutt, B.; Saraswat, K. C. (2013). Approaches for a viable Germanium laser: Tensile strain, GeSn alloys, and n-type doping. Optical Interconnects Conference, 2013 IEEE.

[24] Cho, Y. J.; Kim, C. H.; Im, H. S.; Myung, Y.; Kim, H. S.; Back, S. H.; Lim, Y. R.; Jung, C. S.; Jang, D. M.; Park, J.; Lim, S. H.; Cha, E. H.; Bae, K. Y.; Song, M. S.; Cho, W. I. Germanium-tin alloy nanocrystals for high-performance lithium ion batteries. *Phys. Chem. Chem. Phys.* **2013**, *15*, 11691.

[25] Esteves, R. J. A.; Ho, M. Q.; Arachchige, I. U. Nanocrystalline Group IV Alloy Semiconductors: Synthesis and Characterization of Ge1–xSnx Quantum Dots for Tunable Bandgaps. *Chem. Mater.* **2015**, *27*, 1559.

[26] Alan Esteves, R. J.; Hafiz, S.; Demchenko, D. O.; Ozgur, U.; Arachchige, I. U. Ultra-small Ge1-xSnx quantum dots with visible photoluminescence. *Chem. Commun.* **2016**, *52*, 11665.

[27] Ramasamy, K.; Kotula, P. G.; Fidler, A. F.; Brumbach, M. T.; Pietryga, J. M.; Ivanov, S. A. SnxGe1−x Alloy Nanocrystals: A First Step toward Solution-Processed Group IV Photovoltaics. *Chem. Mater.* **2015**, *27*, 4640.

[28] Křenek, T.; Bezdička, P.; Murafa, N.; Šubrt, J.; Pola, J. Laser CVD of Nanodisperse Ge–Sn Alloys Obtained by Dielectric Breakdown of SnH4/GeH4 Mixtures. *Eur. J. Inorg. Chem.* **2009**, *2009*, 1464.

[29] Assali, S.; Dijkstra, A.; Li, A.; Koelling, S.; Verheijen, M. A.; Gagliano, L.; Von Den Driesch, N.; Buca, D.; Koenraad, P. M.; Haverkort, J. E. M.; Bakkers, E. P. a. M. Growth and Optical Properties of Direct Band Gap Ge/Ge0.87Sn0.13 Core/Shell Nanowire Arrays. *Nano Lett.* **2017**, *17*, 1538.

[30] Biswas, S.; Doherty, J.; Saladukha, D.; Ramasse, Q.; Majumdar, D.; Upmanyu, M.; Singha, A.; Ochalski, T.; Morris, M. A.; Holmes, J. D. Non-equilibrium induction of tin in germanium: towards direct bandgap Ge1−xSnx nanowires. *Nat. Commun.* **2016**, *7*, 11405.

[31] Biswas, S.; Barth, S.; Holmes, J. D. Inducing imperfections in germanium nanowires. *Nano Res.* **2017**, *10*, 1510.

[32] Seifner, M. S.; Biegger, F.; Lugstein, A.; Bernardi, J.; Barth, S. Microwave-Assisted Ge1−xSnx Nanowire Synthesis: Precursor Species and Growth Regimes. *Chem. Mater.* **2015**, *27*, 6125.

[33] Barth, S.; Seifner, M. S.; Bernardi, J. Microwave-assisted solution-liquid-solid growth of Ge1-xSnx nanowires with high tin content. *Chem. Commun.* **2015**, *51*, 12282.

[34] Lan, H. S.; Chang, S. T.; Liu, C. W. Semiconductor, topological semimetal, indirect semimetal, and topological Dirac semimetal phases of Ge1-xSnx alloys. *Phys. Rev. B* **2017**, *95*, 201201.

[35] Oehme, M.; Kostecki, K.; Schmid, M.; Oliveira, F.; Kasper, E.; Schulze, J. Epitaxial growth of strained and unstrained GeSn alloys up to 25% Sn. *Thin Solid Films* **2014**, *557*, 169.

[36] Gurdal, O.; Desjardins, P.; Carlsson, J. R. A.; Taylor, N.; Radamson, H. H.; Sundgren, J. E.; Greene, J. E. Low-temperature growth and critical epitaxial thicknesses of fully strained metastable Ge1−xSnx (x≲0.26) alloys on Ge(001)2×1. *J. Appl. Phys.* **1998**, *83*, 162.

[37] He, G.; Atwater, H. A. Synthesis of epitaxial SnxGe1−x alloy films by ion-assisted molecular beam epitaxy. *Appl. Phys. Lett.* **1996**, *68*, 664.

[38] Shigeaki, Z.; Osamu, N.; Noriyuki, T.; Masashi, K.; Wakana, T.; Mitsuo, S. Growth and applications of GeSn-related group-IV semiconductor materials. *Sci. Technol. Adv. Mater.* **2015**, *16*, 043502.

[39] Taoka, N.; Capellini, G.; Schlykow, V.; Montanari, M.; Zaumseil, P.; Nakatsuka, O.; Zaima, S.; Schroeder, T. Electrical and optical properties improvement of GeSn layers formed at high temperature under well-controlled Sn migration. *Mater. Sci. Semicond. Process* **2017**, *57*, 48.

[40] Grzybowski, G.; Beeler, R. T.; Jiang, L.; Smith, D. J.; Kouvetakis, J.; Menéndez, J. Next generation of Ge1−ySny (y = 0.01-0.09) alloys grown on Si(100) via Ge3H8 and SnD4: Reaction kinetics and tunable emission. *Appl. Phys. Lett.* **2012**, *101*, 072105.

[41] Roskamp, C. A.; Roskamp, E. J. (2001). Germanium Dichloride–Dioxane Complex. Encyclopedia of Reagents for Organic Synthesis, John Wiley & Sons, Ltd.

[42] Lappert, M. F.; Power, P. P. (1976). Di- and Trivalent Trimethylsilyl-Substituted Tin Amides and Related Compounds Such as Sn[N(SiMe3)2]2. Organotin Compounds: New Chemistry and Applications, AMERICAN CHEMICAL SOCIETY. 157: 70.

[43] Vnuk, F.; De Monte, A.; Smith, R. W. The effect of pressure on the semiconductor-to-metal transition temperature in tin and in dilute Sn–Ge alloys. *J. Appl. Phys.* **1984**, *55*, 4171.

[44] Hochst, H.; Engelhardt, M. A.; R. C. Bowman, J.; Adams, P. M. Characterisation of MBE-grown α-Sn films and α-Sn 1-x Ge x alloys. *Semicond. Sci. Technol.* **1990**, *5*, S240.

[45] Farrow, R. F. C.; Robertson, D. S.; Williams, G. M.; Cullis, A. G.; Jones, G. R.; Young, I. M.; Dennis, P. N. J. The growth of metastable, heteroepitaxial films of α-Sn by metal beam epitaxy. *J. Cryst. Growth* **1981**, *54*, 507.

[46] Im, H. S.; Cho, Y. J.; Lim, Y. R.; Jung, C. S.; Jang, D. M.; Park, J.; Shojaei, F.; Kang, H. S. Phase Evolution of Tin Nanocrystals in Lithium Ion Batteries. *ACS Nano* **2013**, *7*, 11103.

[47] Bauer, M.; Taraci, J.; Tolle, J.; Chizmeshya, A. V. G.; Zollner, S.; Smith, D. J.; Menendez, J.; Hu, C.; Kouvetakis, J. Ge–Sn semiconductors for band-gap and lattice engineering. *Appl. Phys. Lett.* **2002**, *81*, 2992.

[48] Beeler, R.; Roucka, R.; Chizmeshya, A. V. G.; Kouvetakis, J.; Menéndez, J. Nonlinear structure-composition relationships in the Ge1-ySny/Si(100) (y<0.15) system. *Phys. Rev. B* **2011**, *84*, 035204.

[49] Gencarelli, F.; Grandjean, D.; Shimura, Y.; Vincent, B.; Banerjee, D.; Vantomme, A.; Vandervorst, W.; Loo, R.; Heyns, M.; Temst, K. Extended X-ray absorption fine structure investigation of Sn local environment in strained and relaxed epitaxial Ge1−xSnx films. *J. Appl. Phys.* **2015**, *117*, 095702.

[50] Lin, H.; Chen, R.; Huo, Y.; Kamins, T. I.; Harris, J. S. Raman study of strained Ge1−xSnx alloys. *Appl. Phys. Lett.* **2011**, *98*, 261917.

[51] D'costa, V. R.; Tolle, J.; Roucka, R.; Poweleit, C. D.; Kouvetakis, J.; Menéndez, J. Raman scattering in Ge1−ySny alloys. *Solid State Commun.* **2007**, *144*, 240.

[52] Li, S. F.; Bauer, M. R.; Menéndez, J.; Kouvetakis, J. Scaling law for the compositional dependence of Raman frequencies in SnGe and GeSi alloys. *Appl. Phys. Lett.* **2004**, *84*, 867.

[53] Su, S.; Wang, W.; Cheng, B.; Hu, W.; Zhang, G.; Xue, C.; Zuo, Y.; Wang, Q. The contributions of composition and strain to the phonon shift in Ge₁–xSnx alloys. *Solid State Commun.* **2011**, *151*, 647.

[54] Sanchez-Soares, A.; Greer, J. C. A Semimetal Nanowire Rectifier: Balancing Quantum Confinement and Surface Electronegativity. *Nano Lett.* **2016**, *16*, 7639.

[55] Von Den Driesch, N.; Stange, D.; Wirths, S.; Mussler, G.; Holländer, B.; Ikonic, Z.; Hartmann, J. M.; Stoica, T.; Mantl, S.; Grützmacher, D.; Buca, D. Direct Bandgap Group IV Epitaxy on Si for Laser Applications. *Chem. Mater.* **2015**, *27*, 4693.

[56] Moutanabbir, O.; Isheim, D.; Blumtritt, H.; Senz, S.; Pippel, E.; Seidman, D. N. Colossal injection of catalyst atoms into silicon nanowires. *Nature* **2013**, *496*, 78.

[57] Moutanabbir, O.; Senz, S.; Scholz, R.; Alexe, M.; Kim, Y.; Pippel, E.; Wang, Y.; Wiethoff, C.; Nabbefeld, T.; Meyer Zu Heringdorf, F.; Horn-Von Hoegen, M. Atomically Smooth p-Doped Silicon Nanowires Catalyzed by Aluminum at Low Temperature. *ACS Nano* **2011**, *5*, 1313.

[58] Wen, C. Y.; Tersoff, J.; Reuter, M. C.; Stach, E. A.; Ross, F. M. Step-Flow Kinetics in Nanowire Growth. *Phys. Rev. Lett.* **2010**, *105*, 195502.

[59] Gamalski, A. D.; Ducati, C.; Hofmann, S. Cyclic Supersaturation and Triple Phase Boundary Dynamics in Germanium Nanowire Growth. *J. Phys. Chem. C* **2011**, *115*, 4413.

[60] Feutelais, Y.; Legendre, B.; Fries, S. G. Thermodynamic evaluation of the system germanium — tin. *Calphad* **1996**, *20*, 109.

[61] Zhang, Y. M.; Evans, J. R. G.; Yang, S. The prediction of solid solubility of alloys: developments and applications of Hume-Rothery's rules. *J. Cryst. Phys. Chem.* **2010**, *1*, 103.

[62] Barrio, R. A.; Querales Flores, J. D.; Fuhr, J. D.; Ventura, C. I. Non-substitutional Sn Defects in Ge₁–x Sn x Alloys for Opto- and Nanoelectronics. *J. Supercond. Novel Magn.* **2013**, *26*, 2213.

[63] Asom, M. T.; Kortan, A. R.; Kimerling, L. C.; Farrow, R. C. Structure and stability of metastable α-Sn. *Appl. Phys. Lett.* **1989**, *55*, 1439.

[64] Wang, B.; Ouyang, G.; Yang, Y. H.; Yang, G. W. Anomalous thermal stability of cubic tin confined in a nanotube. *Appl. Phys. Lett.* **2007**, *90*, 121905.

[65] Matsumura, R.; Chikita, H.; Kai, Y.; Sadoh, T.; Ikenoue, H.; Miyao, M. Low-temperature (∼180 °C) position-controlled lateral solid-phase crystallization of GeSn with laser-anneal seeding. *Appl. Phys. Lett.* **2015**, *107*, 262106.

[66] Park, J.-H.; Tada, M.; Kapur, P.; Peng, H.; Saraswat, K. C. Self-nucleation free and dimension dependent metal-induced lateral crystallization of amorphous germanium for single crystalline germanium growth on insulating substrate. *J. Appl. Phys.* **2008**, *104*, 064501.

[67] Tauc, J. Optical properties and electronic structure of amorphous Ge and Si. *Mater. Res. Bull.* **1968**, *3*, 37.

[68] Tauc, J.; Grigorovici, R.; Vancu, A. Optical Properties and Electronic Structure of Amorphous Germanium. *Phys. Status Solidi B* **1966**, *15*, 627.

Table of Contents artwork